Normal and oblique droplet impingement dynamics on moving dry walls

K. Ashoke Raman[*]

Department of Mechanical Engineering, National University Singapore, 10 Kent Ridge Crescent, Singapore 117576, Singapore

Industrial applications that depend on jetting-based technology, such as painting or additive layered manufacturing, involve sequential deposition of droplets onto a moving surface. Spreading and receding dynamics of these impinging drops depend on the momentum transferred by the moving wall to the droplet liquid, which in turn governs the geometric precision and surface finish of the printed outcome. In this work, the impingement dynamics of microdroplets on a flat, smooth, and moving solid surface is computed using a phase-field-based lattice Boltzmann method. Moreover, the motion of the three-phase moving contact line is captured using a geometry-based contact angle formulation. First, we investigate the influence of various process and materials parameters such as wall velocity, droplet viscosity, surface tension, and wettability on the impact behavior of drops. The surface wettability significantly affects the droplet morphology; an elongated tail like structure forms on the rear end of the droplet which becomes sharper as the moving surface becomes more hydrophobic. Furthermore, we examine the underlying flow physics of the symmetry breaking during the spreading and recoiling phases. For a given contact angle, an increase in wall velocity is found to expedite droplet spreading. In addition, for the first time we explore the oblique droplet impingement dynamics on moving dry walls in this work. It is observed that wall momentum affects the structure of the leading edge during the *inline* impact situations, whereas the moving surface controls the delay in flow reversal inside the droplet for *opposing* impact scenarios.

I. INTRODUCTION

Interactions between falling droplets with a moving solid surface are ubiquitous in nature and form the governing elemental step in several industrial applications. In everyday situations, such as standing in a shower or rain drops splashing on the windshield of a moving car, we observe this commonly occurring phenomenon of droplet impingement on moving surfaces. As such, the intricate interplay the surface tension forces, droplet viscosity, fluid inertia, and wall momentum leading to different morphological structures evolving spatiotemporally often goes unnoticed. However, the understanding of the fluid dynamical aspects of these interactions becomes pivotal in droplet-based industrial applications such as the impact of ink droplets on a moving sheet of paper; spray painting and cooling over a moving surface; fuel droplets impacting on a moving piston; and jetting-based additive manufacturing technology [1], where the geometrical precision and surface finish of the additive layers is controlled by droplet-wall interactions. In jetting technology, a train of droplets impacts onto a moving surface as they are deposited side by side, making up the additive layer. The impingement dynamics not only depend on the physical and chemical properties of the droplet but also on the motion of the target surface. It is this coupled interaction between the supplied wall momentum and the impacting droplet which determines the overall impingement dynamics. A basic understanding of this interaction process and insights of the underlying flow mechanisms for varying conditions are essential for

improving the geometrical precision of the desired product. How does a droplet evolve spatiotemporally when impinged onto a moving solid surface? We set out to investigate this question in the current work.

Due to its relevance in both nature and technological applications such as ink-jet printing, spray cooling and painting, microfabrication, fuel spray in combustion chambers, and enhanced oil recovery, to mention a few, researchers have always been intrigued about understanding the underlying rapid dynamics of droplet impact on solid surfaces. Worthington [2] was the first to investigate this phenomenon systematically, and different aspects of droplet impaction have been investigated using theory [3–5], experiments [6–9], and numerical simulations [10–13]. Comprehensive reviews elucidating the important dynamical aspects of the impact process of a single droplet on stationary thin films and drywall are presented in the review articles provided by Yarin [9] and Rein [14]. While different impact outcomes are observed, such as *complete rebound*, *partial rebound*, and *receding breakup*, when a droplet impacts onto a stationary surface, a distinct similarity in most of these outcomes is the presence of symmetric morphological features and flow field inside the drop during its spreading and receding phases. Situations in which the symmetry in the flow field and droplet shape is broken as it impacts a stationary solid surface arise due to inhomogeneities in chemical properties [15–17] and roughness of the target surface [18–20]. Raman *et al.* [15] performed three-dimensional lattice Boltzmann simulations to investigate droplet impact on solid surfaces exhibiting a gradient in the surface contact angle. They observed that the motion of the droplet is characterized by intense recoiling of the upstream end of the droplet followed by the secondary

———————
[*]ashokeraman@gmail.com

spreading of the downstream end. A droplet impinging normally onto a textured hydrophobic surface with a gradient in surface roughness is observed to bounce off obliquely from the substrate [19]. Such behavior is attributed to the transfer of vertical momentum into the horizontal direction. Experiments performed by Vaikuntanathan *et al.* [18] of droplet impact onto the junction line between the hydrophobic textured and the hydrophilic smooth portions of a dual-textured substrate revealed that the initial droplet spreading is unaffected by the dual-textured feature of the substrate. However, the net movement of the droplet onto the hydrophilic region is noted due to intense recoiling speeds. More recently, Zhao and Chen [20] simulated droplet impact on micropatterned surfaces using many-body dissipative particle dynamics. They demonstrated that a nonuniform spacing between the pillars leads to the coexistence of the Cassie and Wenzel states which causes the droplet to migrate against the wettability gradient. If the surface is smooth with a constant contact angle, then asymmetry in the shape of the impinging droplet is observed when the target surface is subjected to mechanical motion.

Unlike the extensive literature available on droplet impact onto stationary surfaces, there are few works investigating the dynamics of an impinging drops on moving dry [21–23] and wet walls [24–26]. Xie *et al.* [24] performed a three-dimensional numerical investigation of droplet impact on flowing films. A control-volume finite-element method-based solver with adaptive unstructured meshes was employed in their study. For an air-water system, the impacting drop was characterized by a horseshoelike structure at the leading end, whereas the trailing part developed into an elongated tail. Several dimples characterize the air-water interface at the trailing end before the droplet system breaks into several liquid filaments and droplets. However, for the steam-water system, the droplet has a canopy-shaped frontal end with no formation of the long tail, and only one single large dimple was formed as the droplet touches the base film. Ming and Jing [25] observed asymmetric splashing when a droplet impacts normally onto a moving wall covered by a thin film. While splashing is enhanced in the direction opposite to the wall motion, it is observed that lamella growth is attenuated in the streamwise direction. This suppression effect in the streamwise direction becomes more evident with increasing wall velocity. The velocity distribution near the tip of the crown on the downstream side was found to be asymmetric. Similarly, asymmetry in droplet morphology in the form of an inclined central jet is observed by Raman *et al.* [26] when two droplets impact simultaneously on moving thin films. The momentum flux supplied by the moving liquid or film to the impacting droplet in a given direction leads to this asymmetry in velocity distribution and surface morphology. Also, there is a constant supply of liquid from the film into the evolving ejecta, the magnitude of which depends on its moving velocity. On moving dry walls, the impact behavior of the droplet is governed by the motion of the three-phase contact line relative to the moving surface. Bird *et al.* [22] observed symmetry breaking when an ethanol drop impacts onto a moving aluminum surface. The portion of the lamella moving along the wall continued to spread over the wall. However, the upstream lamella moving into the opposite direction delaminated from the surface and was airborne,

resulting in splashing. The amount of liquid detaching from the moving wall increases with the increase in wall velocity [27]. This asymmetric droplet splashing behavior on dry walls is found to be dependent monotonically on droplet speed, diameter, substrate speed, and ambient pressure [21]. Corona splash is found to be entirely suppressed by reducing ambient pressure. However, the droplet viscosity exhibited a nonmonotonic effect on the splashing threshold. A splashing mechanism on a moving surface and on an inclined surface were found to be different by Zen *et al.* [28], as the effect of gravity suppressed upstream splash on an inclined surface. More recently, Almohammadi and Amirfazli [23] found that the wettability of the moving surface significantly affects the downstream behavior of the lamella and the droplet splashing is azimuthally asymmetric. Hydrophobic moving surfaces favor larger delamination of the lamella from the surface when compared with a hydrophilic surface. An asymmetric break-up of the flow field inside the impacting drop has been found to suppress droplet rebounding off a hydrophobic surface [29].

From the significantly few studies related to droplet impaction onto moving dry walls, it is found that the central focus of these investigations has been on the outcome of droplet *splashing*. Almost all existing works have not considered the role of the moving substrate on droplet *deposition* and *rebound* outcomes, situations which are encountered in ink-jet printing and jetting-based additive manufacturing [1]. In contrast to droplet *splashing*, where the primary interest of investigation is the ejecting lamella, the understanding of the morphology and dynamics of the entire droplet system is necessary to obtain the desired geometrical precision in these applications. Therefore in this work, we set out to fill the following gaps of knowledge. First, we investigate droplet *deposition* and *rebound* impact outcomes by providing a systematic numerical study of the droplet impact on a moving solid surface with different wettabilities. In order to elucidate the underlying physical mechanisms, the energetics of spreading and recoiling phases have been investigated by monitoring surface energy evolution, whereas flow-field dynamics inside the droplet is explored to analyze symmetry breaking. Second, the authors know of no prior research on oblique droplet impact onto moving dry walls. In many practical situations, the impact is not normal to the target surface, and the alignment of the line of impact with respect to the translational direction of the moving surface is essential to consider. We investigate both the inline and opposing oblique droplet impact scenarios in this study for the first time.

The remainder of the paper is organized as follows: The problem setup along with the details of the computational domain and the applied boundary conditions are outlined in Sec. II. Section III describes the system of equations governing the phase-field lattice Boltzmann model. The geometry-based contact angle model is introduced in this section. We then proceed with the presentation of the results and discussions in Sec. IV. Concluding remarks are provided in Sec. V.

II. PROBLEM STATEMENT

A sketch outlining the problem definition is provided in Fig. 1. The droplet and the surrounding fluid are considered to be incompressible, viscous, and immiscible. The droplet
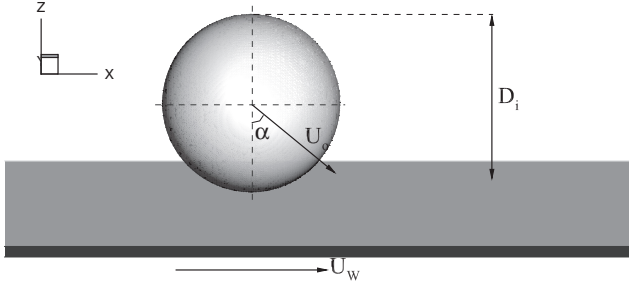
FIG. 1. A schematic representation of a droplet with diameter D_i, impacting on a moving dry wall. The angle of impingement is α and the wall moves with a constant translational velocity U_w along the positive x direction.

density and viscosity are denoted by ρ_l and μ_l, respectively, while those of the surrounding fluid are represented by ρ_g and μ_g. The effects of gravity are considered to be negligible, and the surface tension coefficient is assumed to be constant. A droplet of diameter D_i impinges onto a solid surface with an impact velocity and impingement angle of U_i and α, respectively. The solid surface moves with a constant translational wall velocity of U_w. All the length and velocity scales are made nondimensional by the initial droplet diameter (D_i) and the impact velocity (U_o), respectively. Accordingly, the nondimensional time is given as $T^* = tD_i/U_o$, where t is the simulation time in lattice units. Important dimensionless parameters governing droplet impact on solid substrate include the Weber number, We $= \rho_l U_o^2 D_i/\sigma$, which indicates the ratio of inertial force to surface tension; the Reynolds number, Re $= \rho_l U_o D_i/\mu_l$, which denotes the ratio of inertial force to viscous force; the density ratio, $\rho_r = \rho_l/\rho_r$; and viscosity ratio, $\mu_r = \mu_l/\mu_g$. The density ratio and viscosity ratio in the current work are set to be $\rho_r = 1000$ and $\mu_r = 40$, respectively. The realistic dimensions of the droplets considered in this study are in micrometers, as illustrated in the experimental validation of this solver [29]. Hence, the influence of gravity in this study is considered to be negligible since the radius of droplet is smaller than the capillary length. The resulting Bond number for the impacting droplet on the moving wall would be of the order of $O(10^{-4})$. To investigate the role of surface movement and wettability, we set the Reynolds number and the Weber number of the impinging droplet at Re $= 600$ and We $= 51.2$, respectively. The computational domain is a cuboid with its nondimensional size set to be $6.44 \times 2.44 \times 1.72$. The no-slip wall boundary conditions are applied on the top and bottom boundary. For the bottom boundary, the no-slip boundary condition is imposed using the bounce back scheme [30] in which the colliding particles not only reverse their momenta but also gain momentum due to the wall velocity U_w. Periodic boundary conditions are imposed on the side boundaries.

III. MATHEMATICAL FORMULATION

To understand the interaction dynamics between a wall impinging drop and a moving dry wall, we employ the phase-field-based lattice Boltzmann method [31–34]. Two particle

distribution functions are used in this model [31] to recover the incompressible Navier-Stokes equation (g_α) and a macro interface capturing phase-field equation (f_α). The model consists of stress and potential forms of intermolecular forcing terms in the momentum equation and the phase-field model for the order parameter, respectively. Stable discretization schemes are considered to discretize the forcing terms in each collision step, which helps in improving numerical stability for high-density ratio cases. The discrete Boltzmann equation (DBE) for pressure and momentum is expressed as:

$$
\begin{aligned}
&\frac{\partial g_\alpha}{\partial t} + e_{\alpha i}\frac{\partial g_\alpha}{\partial x_i} \\
&= -\frac{(g_\alpha - g_\alpha^{\text{eq}})}{\lambda} + \frac{(e_{\alpha i} - u_i)\partial_i(\rho c_s^2)}{c_s^2}[\Gamma_\alpha(\mathbf{u}) - \Gamma_\alpha(0)] \\
&\quad + \frac{(e_{\alpha i} - u_i)[\kappa\partial_i(\partial_k\rho\partial_k\rho) - \kappa\partial_j(\partial_j\partial_i\rho)]}{c_s^2}\Gamma_\alpha(\mathbf{u}),\quad (1)
\end{aligned}
$$

where λ is the relaxation time due to collision and e_α is the microscopic particle velocity. The corresponding DBE for the order parameter is given as

$$
\begin{aligned}
&\frac{\partial f_\alpha}{\partial t} + e_{\alpha i}\frac{\partial f_\alpha}{\partial x_i} \\
&= -\frac{(f_\alpha - f_\alpha^{\text{eq}})}{\lambda} \\
&\quad + \frac{(e_{\alpha i} - u_i)[\partial_i(\rho c_s^2) - \rho\partial_i(\phi - \kappa\partial_j^2\rho)]}{c_s^2}\Gamma_\alpha(\mathbf{u}),\quad (2)
\end{aligned}
$$

where $\tau = \lambda/\delta t$.

The equilibrium distribution functions are given by

$$
f_\alpha^{\text{eq}} = w_\alpha\rho\left[1 + \frac{\mathbf{e}_\alpha.\mathbf{u}}{c_s^2} + \frac{(\mathbf{e}_\alpha.\mathbf{u})^2}{2c_s^4} - \frac{(\mathbf{u}.\mathbf{u})}{2c_s^2}\right],\quad (3)
$$

$$
g_\alpha^{\text{eq}} = w_\alpha\left[\frac{p}{c_s^2} + \frac{\rho\mathbf{e}_\alpha.\mathbf{u}}{c_s^2} + \frac{\rho(\mathbf{e}_\alpha.\mathbf{u})^2}{2c_s^4} - \frac{\rho(\mathbf{u}.\mathbf{u})}{2c_s^2}\right],\quad (4)
$$

where $c_s = 1/\sqrt{3}$ and w_α are the corresponding integral weights for a D3Q19 lattice velocity model:

$$
\begin{aligned}
w_\alpha &= \tfrac{1}{3}, \quad \alpha = 0 \\
w_\alpha &= \tfrac{1}{18}, \quad \alpha \in [1, 6] \\
w_\alpha &= \tfrac{1}{36}, \quad \alpha \in [7, 18]
\end{aligned}\quad (5)
$$

and

$$
\Gamma_\alpha(\mathbf{u}) = w_\alpha\left[1 + \frac{\mathbf{e}_\alpha.\mathbf{u}}{c_s^2} + \frac{(\mathbf{e}_\alpha.\mathbf{u})^2}{2c_s^4} - \frac{(\mathbf{u}.\mathbf{u})}{2c_s^2}\right].\quad (6)
$$

These two equations are discretized along the characteristics over a time step δt. The trapezoidal rule is employed for time integration in $[t, t + \delta t]$ which is coupled with the space integration in $(\mathbf{x} + \mathbf{e}_\alpha\delta t, t + \delta t)$. The resulting lattice Boltzmann equations are solved in three steps:

(i) Prestreaming step

$$\bar{g}_\alpha(\mathbf{x}, t) = g_\alpha(\mathbf{x}, t) - \left.\frac{g_\alpha - g_\alpha^{\text{eq}}}{2\tau}\right|_{(\mathbf{x},t)} + \frac{\delta t}{2} \frac{(e_{\alpha i} - u_i)\partial_i(\rho c_s^2)}{c_s^2}[\Gamma_\alpha(\mathbf{u}) - \Gamma_\alpha(0)]\Big|_{(\mathbf{x},t)}$$

$$+ \frac{\delta t}{2} \frac{(e_{\alpha i} - u_i)[\kappa \partial_i(\partial_k \rho \partial_k \rho) - \kappa \partial_j(\partial_j \rho \partial_i \rho)]}{c_s^2}\Gamma_\alpha(\mathbf{u})\Big|_{(\mathbf{x},t)}, \tag{7}$$

$$\bar{f}_\alpha(\mathbf{x}, t) = f_\alpha(\mathbf{x}, t) - \left.\frac{f_\alpha - f_\alpha^{\text{eq}}}{2\tau}\right|_{(\mathbf{x},t)} + \frac{\delta t}{2} \frac{(e_{\alpha i} - u_i)[\partial_i(\rho c_s^2) - \rho \partial_i(\phi - \kappa \partial_j^2 \rho)]}{c_s^2}\Gamma_\alpha(\mathbf{u})\Big|_{(\mathbf{x},t)}. \tag{8}$$

(ii) Streaming

$$\bar{g}(\mathbf{x} + \mathbf{e}_\alpha \delta t, t + \delta t) = \bar{g}_\alpha(\mathbf{x}, t), \tag{9}$$

$$\bar{f}(\mathbf{x} + \mathbf{e}_\alpha \delta t, t + \delta t) = \bar{f}_\alpha(\mathbf{x}, t). \tag{10}$$

(iii) Poststreaming step

$$g_\alpha(\mathbf{x} + \mathbf{e}_\alpha \delta t, t + \delta t) = \bar{g}_\alpha(\mathbf{x} + \mathbf{e}_\alpha \delta t, t + \delta t) - \frac{1}{2\tau + 1}\left(\bar{g}_\alpha - \bar{g}_\alpha^{\text{eq}}\right)\Big|_{(\mathbf{x} + \mathbf{e}_\alpha \delta t, t + \delta t)}$$

$$+ \frac{2\tau}{2\tau + 1} \frac{\delta t}{2} \frac{(e_{\alpha i} - u_i)\partial_i(\rho c_s^2)}{c_s^2}[\Gamma_\alpha(\mathbf{u}) - \Gamma_\alpha(0)]\Big|_{(\mathbf{x} + \mathbf{e}_\alpha \delta t, t + \delta t)}$$

$$+ \frac{2\tau}{2\tau + 1} \frac{\delta t}{2} \frac{(e_{\alpha i} - u_i)[\kappa \partial_i(\partial_k \rho \partial_k \rho) - \kappa \partial_j(\partial_j \rho \partial_i \rho)]}{c_s^2}\Gamma_\alpha(\mathbf{u})\Big|_{\mathbf{x} + \mathbf{e}_\alpha \delta t, t + \delta t}, \tag{11}$$

$$f_\alpha(\mathbf{x} + \mathbf{e}_\alpha \delta t, t + \delta t) = \bar{f}_\alpha(\mathbf{x} + \mathbf{e}_\alpha \delta t, t + \delta t) - \frac{1}{2\tau + 1}\left(\bar{f}_\alpha - f_\alpha^{\text{eq}}\right)\Big|_{(\mathbf{x} + \mathbf{e}_\alpha \delta t, t + \delta t)}$$

$$+ \frac{2\tau}{2\tau + 1} \frac{\delta t}{2} \frac{(e_{\alpha i} - u_i)[\partial_i(\rho c_s^2) - \rho \partial_i(\phi - \kappa \partial_j^2 \rho)]}{c_s^2}\Gamma_\alpha(\mathbf{u})\Big|_{(\mathbf{x} + \mathbf{e}_\alpha, t + \delta t)}. \tag{12}$$

The chemical potential ϕ is given by

$$\phi \approx 4\beta(\rho - \rho_v^{\text{sat}})(\rho - \rho_l^{\text{sat}})[\rho - \tfrac{1}{2}(\rho_v^{\text{sat}} + \rho_l^{\text{sat}})], \tag{13}$$

where β is a constant and ρ_v^{sat} and ρ_l^{sat} are the saturation densities of the vapor and liquid phases, respectively. The interface thickness, denoted as D, is given by

$$D = \frac{4}{(\rho_l^{\text{sat}} - \rho_v^{\text{sat}})}\sqrt{\frac{\kappa}{2\beta}}, \tag{14}$$

where κ is a constant related to the magnitude of surface tension. The surface tension force σ is represented as

$$\sigma = \frac{(\rho_l^{\text{sat}} - \rho_v^{\text{sat}})^3}{6}\sqrt{2\kappa\beta}. \tag{15}$$

The density of the fluid ρ, hydrodynamics pressure p, and the velocity $\mathbf{u}$ are calculated by taking the moments of the corresponding distribution function:

$$\rho = \sum_\alpha \bar{f}_\alpha, \tag{16}$$

$$p = \sum_\alpha \bar{g}_\alpha c_s^2 + \frac{\delta t}{2} u_i \frac{\partial(\rho c_s^2)}{\partial x_i}, \tag{17}$$

$$u_i = \sum_\alpha \bar{g}_\alpha \mathbf{e}_{\alpha i} + \frac{\delta t}{2}\kappa\left[\frac{\partial}{\partial x_i}\left(\frac{\partial \rho}{\partial x_k}\frac{\partial \rho}{\partial x_k}\right) - \frac{\partial}{\partial x_j}\left(\frac{\partial \rho}{\partial x_i}\frac{\partial \rho}{\partial x_j}\right)\right]. \tag{18}$$

The relaxation parameter τ is related to the kinematic viscosity $\nu = \tau c_s^2 \delta t$, which can be calculated by a linear interpolation

$$\tau = C\tau_l - (1 - C)\tau_v, \tag{19}$$

where τ_l and τ_v are the relaxation times for liquid and vapor, respectively, and the parameter C is the composition approximated by

$$C = \frac{(\rho - \rho_v^{\text{sat}})}{(\rho_l^{\text{sat}} - \rho_v^{\text{sat}})}. \tag{20}$$

The mixed difference scheme and the second-order central difference scheme are considered for discretizing the forcing terms in the prestreaming and poststreaming collision steps, respectively. Further details on the discretization schemes can be found in Ref. [31].

A geometry formulation contact angle proposed by Ding and Spelt [35] is employed to model the three-phase contact line. This geometric scheme also models the contact angle

hysteresis and its applicability on droplet impact problem has been demonstrated [15]. The procedure essentially involves updating the values of the order parameter (density in the present model) to enforce the following equation:

$$\mathbf{n} \cdot \nabla \rho = -\tan\left(\frac{\pi}{2} - \theta\right)|\nabla \rho - (\mathbf{n} \cdot \nabla \rho)\mathbf{n}|. \quad (21)$$

From the above form, we can achieve the desired wettability between the solid and the fluid by specifying the desired contact angle. Once the density on the boundary points is specified, the normal gradient condition in Eq. (21) is satisfied in the solver.

Verification and calibration of the employed 3D solver have been discussed in detail in our previous papers [15,36]. Various benchmark problems such as evaluation of Laplace law for a stationary bubble, determining the static contact angle for droplet resting on surfaces with different wettabilities, and experimental validation for single [37] and consecutive drops [17] impacting droplet on a solid surface were performed. It is important to note that in the current study we employ a constant contact angle model to investigate the droplet-wall interaction dynamics. Unlike the dynamic contact angle model, the model in the present work does not account for the contact line velocity and flow parameters while computing the contact angle. A comprehensive review of various contact line models is discussed in Sui *et al.* [38].

IV. RESULTS AND DISCUSSION

In the following subsections, we will present the numerical results and elucidate the physics of the droplet-wall interactions. The role of surface wettability, wall velocity, droplet viscosity, and impact angle on the interaction dynamics are systematically investigated. We perform a grid independence test by comparing the maximum contact area ($A^*_{\max}$) for droplets impacting with the same initial impact conditions with Re = 600, We = 51.2, $\theta = 90°$, and $U_w = 0.075$. Table I shows $A^*_{\max}$ for three different grid resolutions. Compared to the case with $D_i = 85$ lattice units, only a slight variation of 3.36% in $A^*_{\max}$ is observed for the case with $D_i = 70$ lattice units. Based on the grid independence test, the droplet diameter is set to be 70 lattice units for all the simulations. The simulation is initialized with the droplet placed in contact with the wall such that the distance between the wall and the droplet center is $0.5D_i$.

A. Effect of surface wettability

When a droplet impacts onto a moving surface, the momentum exchange between the droplet-wall system depends

TABLE I. Numerical convergence showing the effect of grid resolution on the maximum contact area ($A^*_{\max}$). Three different droplet radii were considered with the impact conditions being fixed at Re = 600, We = 51.2, $U_w = 0.075$, and $\theta = 90°$.

D_i (in lattice units)	50	70	85
$A^*_{\max}$	3.277	3.705	3.834
Relative error	14.52 %	3.36 %	–

on the volume of droplet liquid in contact with the substrate. One of the factors which govern this transaction is the wettability of the target surface, characterized by the contact angle (θ). Figure 2 illustrates the time evolution snapshots of a single droplet impacting on a dry surface moving with a translational velocity of $U_w = 0.075$. The left and right columns in Fig. 2 correspond to surfaces with $\theta = 90°$ and 140°, respectively. When a drop impacts a surface, a region of high pressure is generated at the point of contact [4] due to the compression of the fluid normal to the solid boundary. This leads to the redirection of the fluid momentum from the normal to the lateral direction, resulting in a pressure decay as the droplet undergoes *inertial spreading*. On a stationary surface, the droplet liquid moves uniformly in all directions, leading to symmetric spreading and recoiling phases. This symmetry is broken when the drop impacts onto a moving surface as shown in Fig. 2 at $T^* = 2.05$. Due to the wall movement, there is a continuous supply of momentum to the spreading droplet liquid near the wall region along the direction of surface motion. This leads to rapid transport and accumulation of the droplet liquid into the downstream rims when compared to the rims in the upstream region of the recoiling droplet. For the case with $\theta = 90°$, we observe a distinct rim in the downstream direction while the upstream rim seems to be merged with the rear end of the droplet. However, for $\theta = 140°$, rims on both sides are clearly visible whose radii of curvature is larger than the case with $\theta = 90°$. As time precedes, the droplet undergoes recoiling and keeps moving forward. A well-defined *tail* like structure is noticed for the case with $\theta = 90°$ at $T^* = 6.85$. This demarcates the droplet into two distinct regions: the rounded *frontal* end with a larger contact area whose size grows due to the accumulation of droplet liquid and the sharper *rearward* end whose *tail* like structure converges as time precedes ($T^* = 12.00$). Absence of such morphological features are noticed for $\theta = 140°$. During the time period between $T^* = 4.1$ to $T^* = 12.00$, we observe the height of the droplet keeps increasing and it eventually lifts off the surface, leading to droplet rebound. However, due to the momentum supplied by the moving wall, the droplet has a horizontal velocity component as it leaves the substrate and takes off obliquely.

As the contact angle decreases, the fluid-substrate free energy increases, leading to greater capillary spreading. This is illustrated from the temporal evolution of the contact area (A^*) with different static contact angles shown in Fig. 3(a). With an increase in θ, the contact area (A^*) of impinging droplet decreases in time. Initially, we observe that the temporal evolution of A^* is independent of θ because the droplet spreading phase is dominated by inertia. As the droplet begins to slow down at the end of the crashing time ($T^* = 1$), the increasing effect of capillary spreading for lower θ results in increasing maximum contact area. For $\theta = 140°$, we observe that A^* converges to zero at $T^* = 9.5$ as the droplet rebounds off the surface. Figure 3(b) illustrates the temporal evolution of the X center of mass (X_m) of the droplet for different contact angles. We observe that X_m decreases as the surface contact angle increases. Moreover, we notice that at a given time instant, the difference in X_m between any two cases increases as time precedes. As the contact area increases, the momentum supplied by the wall to the droplet system
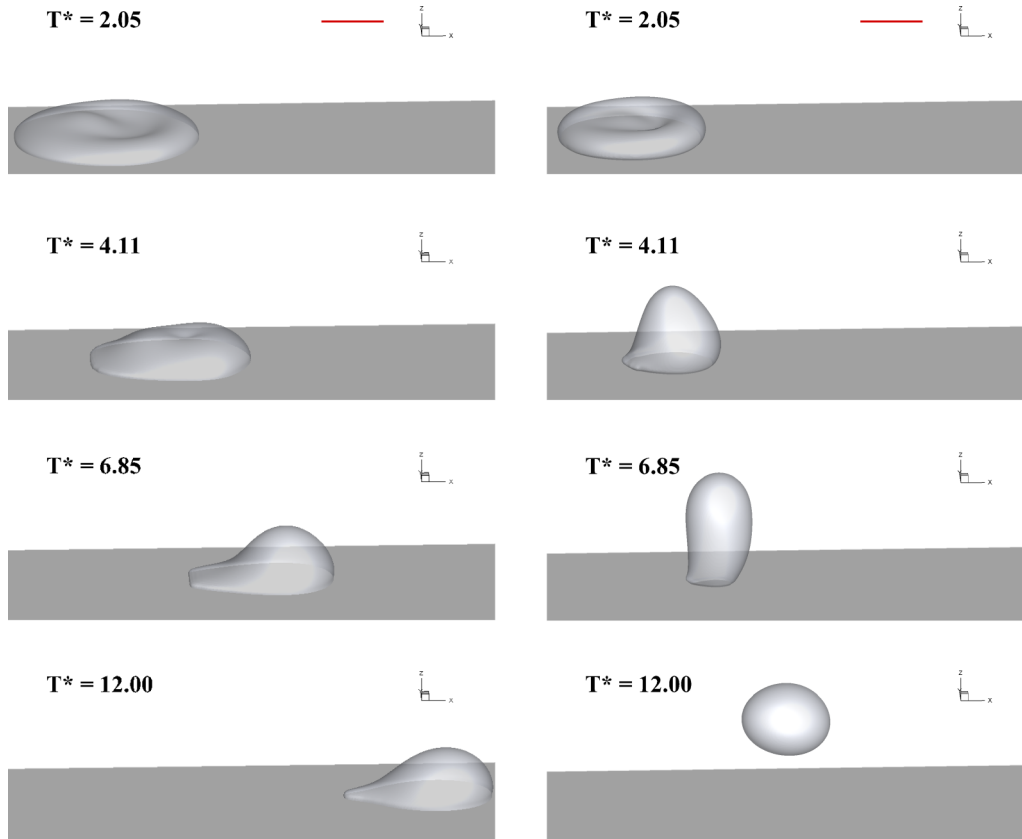
FIG. 2. Temporal sequence of droplet impingement dynamics illustrating the effect surface wettabilities for two different cases: $\theta = 90°$ (left column) and $\theta = 140°$ (right column). For all cases, the wall velocity is fixed at $U_w = 0.075$. The value of the contour density shown in this figure corresponds to $\rho = 0.5(\rho_l + \rho_g)$. Rebound is suppressed for $\theta = 90°$, whereas oblique lift-off from the surface is observed for $\theta = 140°$. The scale bar is 50 lattice units.

increases. This leads to rapid movement of the droplet system along the direction of wall motion. When the contact angle increases, the radius of curvature subtended by the moving contact line increases because the droplet undergoes inertial spreading. This leads to an increase in the surface energy of the spreading rims as more droplet liquid is accumulated inside them, which in turn is converted into kinetic energy when the droplet begins its recoiling phase. Most of this kinetic energy is transferred along the wall-normal direction [29]. However, due to the asymmetry introduced into the droplet system from the momentum supplied by the moving wall, a fraction of this vertical momentum is transferred to the streamwise direction. Fig. 3(c) shows the time evolution of the vertical velocity component of the droplet for different contact angles. As the contact angle increases, the kinetic energy transferred along the z direction increases due to intense recoiling, resulting in a rise in U_z as θ increases. This observation is further elucidated from the interface profiles shown in Fig. 4(a) at $T^* = 6.85$ for different contact angles considered in this section. As we move from left to right, the surface contact angle decreases from $\theta = 140°$ to $70°$. The height of the droplet, at a given time instant, decreases with a decrease in contact angle. The interface profiles vary from being slender and vertically elongated to being tapered and sharp ended as θ decreases. The location of the interface profiles also complements the observations made in Fig. 3(b). The temporal evolution of surface energy (E_σ) illustrated in

Fig. 3(d) shows an increase in E_σ with decreasing θ. This increase in the droplet surface area is attributed to the combined influence of capillary spreading and the resulting increase in the transfer of vertical momentum toward the streamwise direction. Figure 4(b) shows the interface profiles of the contact line footprint for different θ. As contact angle increases, the contact line retracts at a faster recoiling rate. This leads to sharper trailing edges as θ is increased. In contrast, due to the increase in accumulation of the droplet liquid in the *frontal* end, this end becomes increasingly broader and blunt as θ decreases.

While the surface wettability governs the contact area of the impinging droplet, and thereby controls the spreading dynamics on a moving surface, the magnitude of the momentum supplied by the moving wall to the droplet liquid depends on the wall transverse velocity. This, in turn, influences the spreading and receding dynamics of the impacting droplet. We next investigate the influence of wall velocity on the droplet impingement dynamics for a constant contact angle.

B. Wall velocity-induced flow-field asymmetry

Before we begin our investigation on the influence of varying wall velocities, it is imperative to discern the underlying mechanisms of droplet spreading and recoiling between stationary and moving wall scenarios. In order to elucidate the role of wall motion during the inertial spreading phase
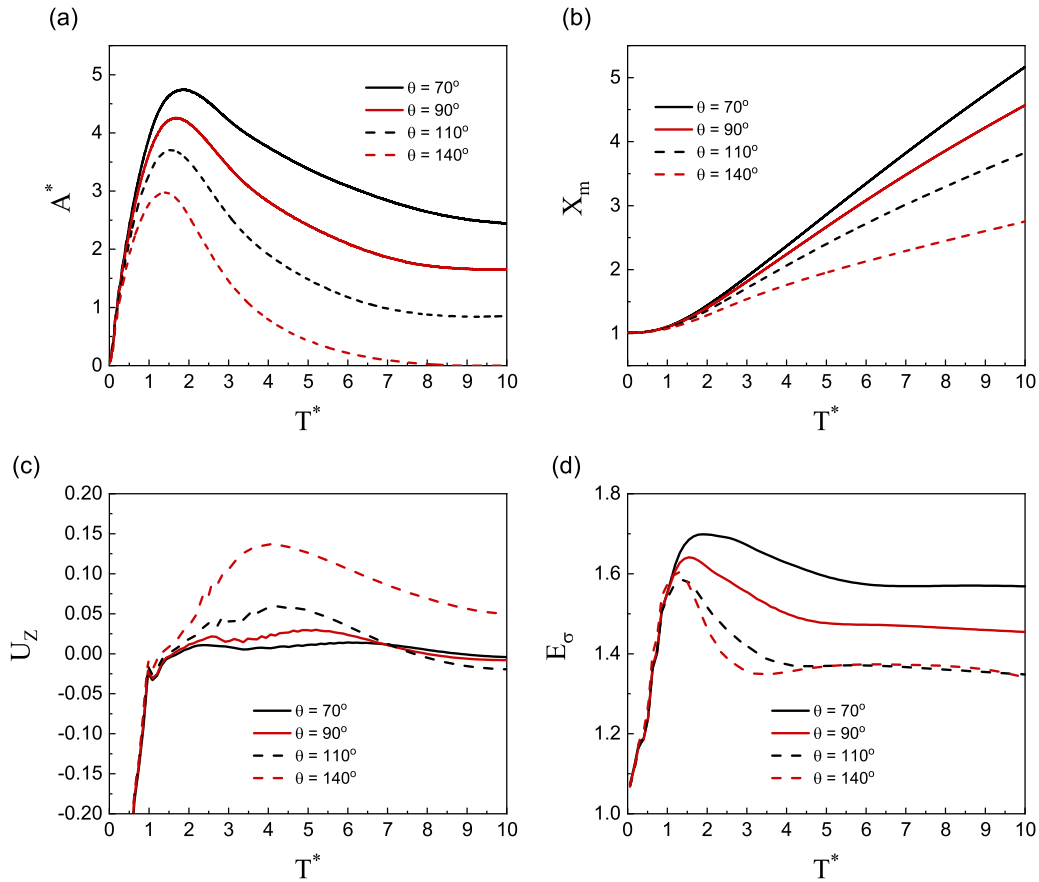
FIG. 3. Temporal evolution of the (a) contact area (A^*), (b) position of the X center of mass (X_m), (c) volume-averaged drop velocity along the wall-normal direction, and (d) surface energy of a droplet impacting onto a target wall moving with a velocity of $U_w = 0.075$ for different surface wettabilities. The contact area and surface energy have been nondimensionalized by $\pi D_i^2/4$ and $\pi D_i^2 \sigma$, respectively. The line colors are assigned as (i) black (online and printed versions), (ii) red (online version), and gray (printed version).

of the droplet impact process, Fig. 5 illustrates the velocity field inside the impinging droplet along the mid-y plane on a stationary (a) and moving [(b) and (c)] surfaces at $T^* = 1.02$. The contact angle for all the situations considered in this section is fixed at $\theta = 110°$. As the droplet impinges onto a stationary surface, the droplet liquid propagates in a radially downward direction leading to the *inertial spreading* phase of the droplet impact. Surface tension forces decelerate this flow propagating radially outward. As a result, the droplet liquid slows down in the peripheral region and begins to get accumu-

lated inside it. The velocity field shown in Fig. 5(a) illustrates this behavior. Although the direction of the velocity field is radially downward and outward for the central and peripheral regions, respectively, a clear contrast in the velocity magnitude is observed between these two regions. It is to be noted that the magnitude of the velocity vectors close to the wall region is nearly zero. Moreover, due to the outward motion of the propagating rim, the velocity field in the surrounding fluid near rim has the same sense of direction. The entire flow field inside the impinging droplet during this *inertial spreading*
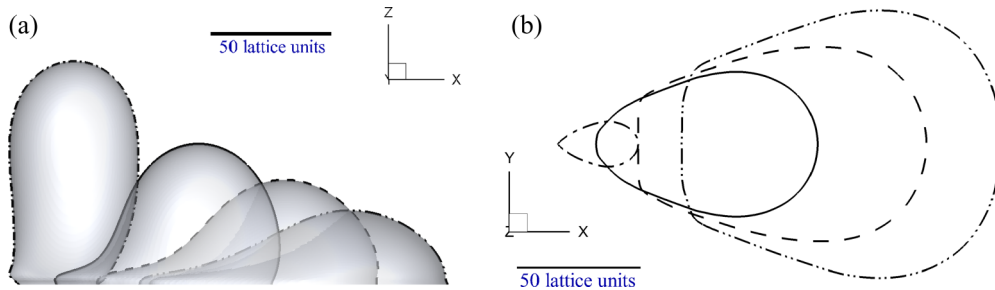
FIG. 4. (a) Instantaneous interface profiles of the impinging droplet along the mid-y plane and (b) the contact line footprint at $T^* = 6.85$ for different contact angles: $\theta = 70°$ (dash dot dot), 90° (dashed), 110° (solid), and 140° (dash dot). The wall is moving with a constant velocity of $U_w = 0.075$. The scale bar is 50 lattice units.
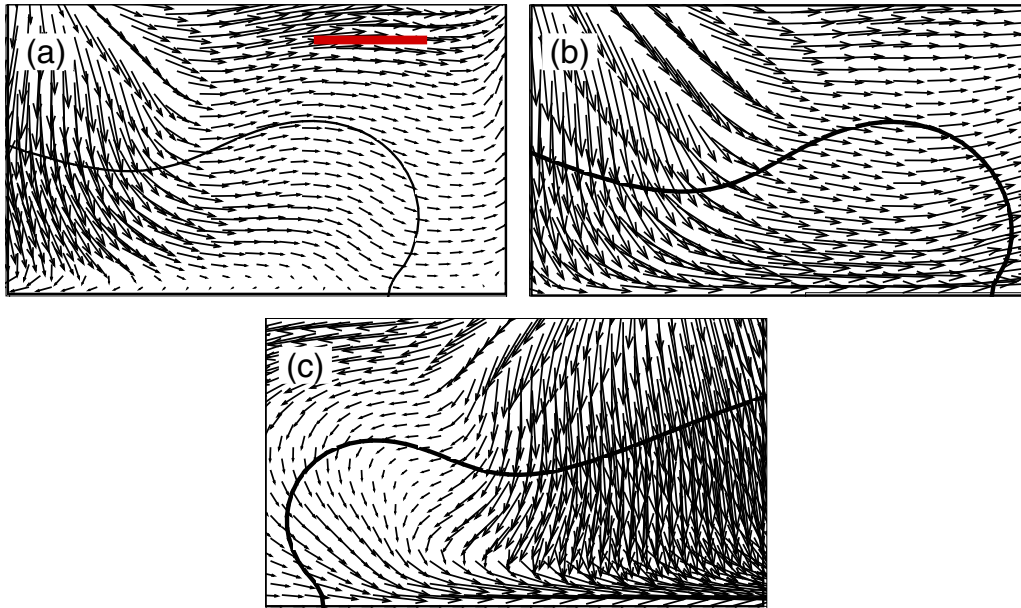
FIG. 5. Instantaneous velocity-field plots inside the peripheral rims of the impacting droplet along the mid-y plane during the *inertial spreading phase* illustrating flow-field symmetry for a stationary wall case with $U_w = 0$ inside the (a) left rim at $T^* = 1.02$. The flow field inside the right rim (not shown here) is symmetrical to that show in (a). Asymmetry in flow field is observed inside the (b) right rim and (c) left rim when a droplet impinges onto a moving surface ($U_w = 0.1$) with $\theta = 110°$. The scale bar is 10 lattice units.

phase is symmetric about the central z axis. This symmetry in velocity field inside the droplet is broken when the wall moves along the x direction with a constant velocity $U_w = 0.1$, as shown in Figs. 5(b) and 5(c). We observe in Fig. 5(b) that the difference in the velocity magnitude between the central and the right peripheral region is much lesser than that observed for the stationary counterpart. This is attributed to the momentum diffusion taking place from the high-velocity fluid close to the wall region, which is observed from the length of the velocity vectors near the wall region, into the fluid layers above it. As a result of this momentum diffusion from the wall region, the velocity fluid inside the right rim is high enough to resist the decelerating effects of surface tension forces in this region. In addition, it is observed from the velocity field that the momentum supplied by the moving wall facilitates in diverting the downward moving flow field in the central region along the direction of wall motion. This additional influx of droplet liquid from the central region into the right rim also attributes to the increase in the velocity magnitude inside this region. Consequently, this has an opposing effect on the flow field inside the left rim as shown in Fig. 5(c). The velocity vectors shows that the high-momentum fluid near the wall region diverts the incoming fluid from the central region of the droplet along the direction of wall motion. This, in turn, expedites the decelerating influence of surface tension forces, leading to a clear difference not only in the magnitude but also in the direction of the velocity field inside the right rim and the central region of the impinging droplet. The direction of the velocity field in the surrounding fluid near the left rim has an opposite sense of direction with that of the fluid inside the rim. With an outward moving right rim and receding left rim, the symmetry of the flow field inside the droplet is broken during the inertial spreading phase of droplet impact on a moving wall.

For the stationary case, by the end of the inertial spreading phase, the droplet reaches its maximum extent of spreading. The kinetic energy of the droplet reaches its minimum, and the surface tension forces begin to dominate, leading to the initiation of droplet recoiling. Figure 6(a) illustrates the velocity field inside the droplet along the mid-y plane at $T^* = 1.71$ during the recoiling phase of the impinging droplet on a stationary wall. We observe that the direction of the velocity field inside the rims is parallel to the surface and opposite to each other, whereas the fluid inside the central region continues to move downward as the central part of the drop continues to undergo spreading. At this time instant, the entire flow field is symmetric along the central z axis with droplet liquid inside the rims and central region propagating radially inward and downward, respectively. On the contrary, the momentum imparted by a moving wall induces a unidirectional flow field inside the droplet as shown in Fig. 6(b). Complemented by the direction of the wall momentum and the restoring effects of surface tension forces, we notice that the flow field inside the left rim moves inward with a higher velocity compared to the right rim, where the decelerating effects of surface tension and wall momentum have opposing effects. This is observed as the magnitude of the velocity field inside the right rim decreases as we move upward along the wall-normal direction. The breakup in the flow-field symmetry is limited not only inside the droplet but also in the surrounding flow field. Two counter-rotating vortices near the peripheral rims are observed in Fig. 6(a) as the droplet recoils, resulting from the drag induced by the receding rims onto the surrounding fluid. However, we observe only a single vortex structure near the left rim as shown in Fig. 6(b).

When an impinging droplet contacts the stationary solid surface, it exhibits radial deformation due to the inertial forces of the droplet liquid. This deformation is characterized by an
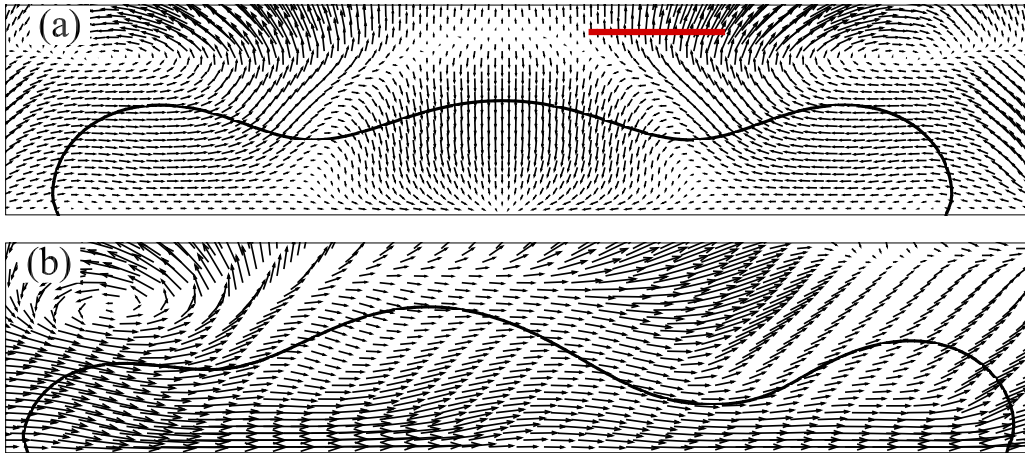
FIG. 6. Instantaneous velocity-field plots inside the impacting droplet along the mid-y plane during the *recoiling phase* illustrating symmetry and asymmetry for (a) $U_w = 0$ and (b) $U_w = 0.1$, respectively, at $T^* = 1.71$. The surface is characterized with a contact angle of $\theta = 110°$ and moves with $U_w = 0.1$. The scale bar is 20 lattice units.

increase of the surface area and variation in the local curvature along the peripheral rims as the droplet liquid accumulates inside it. Thus, a restoring force due to the Laplace pressure acting inside these rims emerges and attempts to dampen the increase in surface area due to inertial forces. The competition between these two opposing forces leads to the generation of capillary waves which travel along the free surface of the droplet. Such capillary waves have also been observed when the shape of the impinging droplet is elliptic at the instant of impact [39] or when the target surface is oscillating [29]. The contour on the left panel of Fig. 7, extracted along the mid-y plane, presents the temporal sequence of the movement of the capillary wave originating close to the peripheral rims due to the competing effects of the decelerating surface tension and inertial forces. The trough of this capillary wave is denoted in red. We observe that the motion of this traveling wave is

symmetric about the central axis and moves in the radially inward direction as the droplet undergoes the recoiling phase. The two troughs of the capillary wave converge ($T^* = 2.4$ and subsequently empty into each other at $T^* = 3.08$. It has been observed in earlier work [39] that when the impact speed is sufficiently high, the collapse of the waves leads to the formation of a small air cavity, which eventually produces the eruption of a thin jet.

When a droplet impacts a moving surface, the momentum diffusing from the moving wall to the droplet liquid leads to a unidirectional flow field inside the drop as illustrated in Fig. 6(b). Hence, the inertial force experienced in the downstream direction is higher than that acting on the upstream rim of the droplet. This leads to an increase in the droplet surface area along the downstream direction which is greater when compared with the upstream part. Subsequently, the
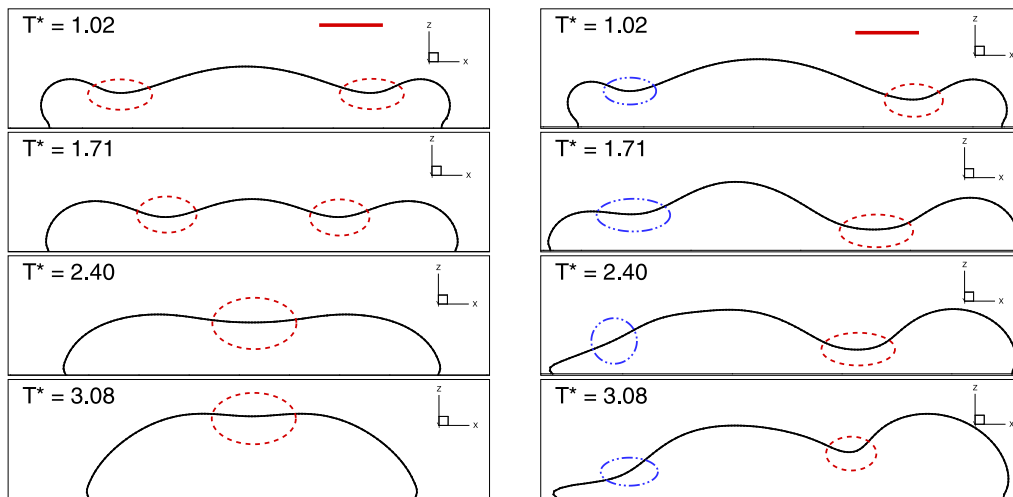
FIG. 7. Motion of the capillary wave moving along the free surface of the droplet when it impact a stationary surface (left column) and a moving surface (right column, $U_w = 0.125$) at different time instants with $\theta = 110°$. Both the troughs of the capillary are marked in red outline (gray dashed line pattern in printed grayscale version) for the stationary wall case, implying the symmetry of the wave. However, the breakdown in this symmetry is highlighted with different colors and line patterns (blue corresponds to dash-dot-dot pattern and red corresponds to dashed pattern) in the case of a moving wall. The scale bar is 20 lattice units.
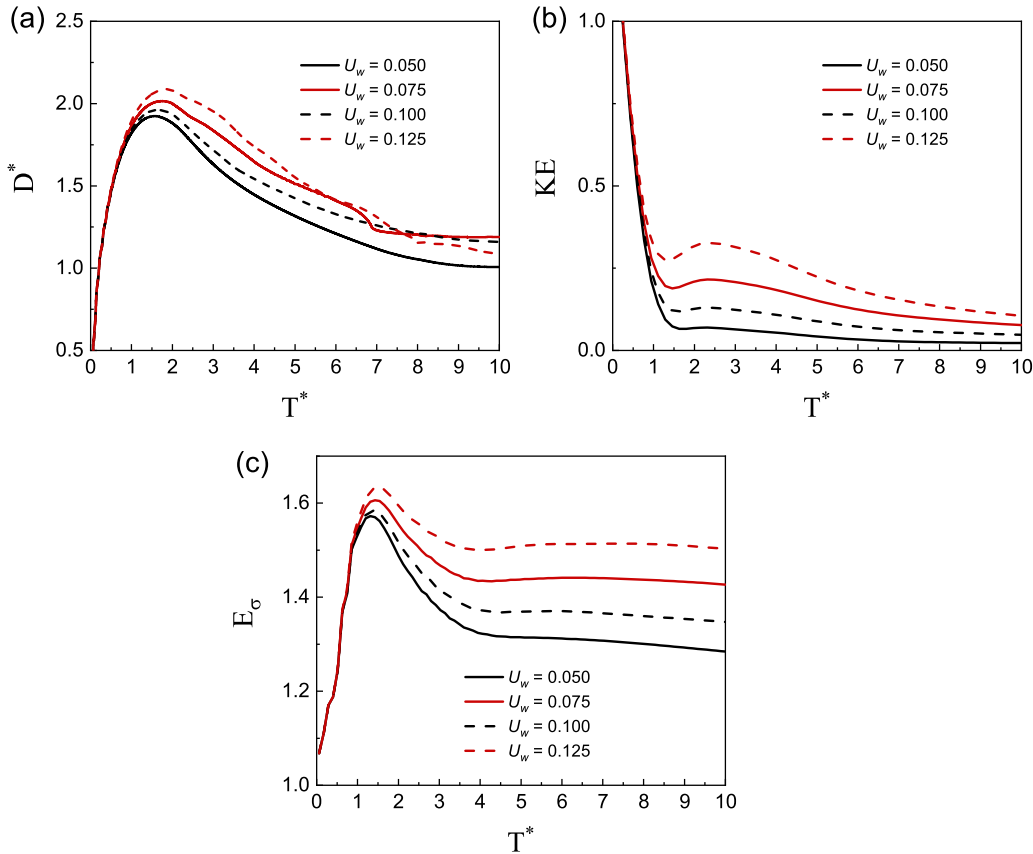
FIG. 8. Temporal evolution of the (a) spread factor (D^*), (b) kinetic energy, and (c) surface energy (E_σ) of a droplet impinging onto a surface with contact angle $\theta = 110°$ moving with different wall velocities. The line colors are assigned as (i) black (online and printed versions), (ii) red (online version), and (iii) gray (printed version).

magnitude of the restoring effects of the interfacial forces acting on these two regions is different. This is observed from the local curvature of the spreading rims as shown in Fig. 7 (right column) at $T^* = 1.02$. As a consequence of these two competing forces, a capillary wave traveling along drop surface is generated having different wave structure and motion near the peripheral rims. The two dissimilar troughs of the traveling capillary wave are marked with different colors as illustrated in Fig. 7 (right column). As the droplet liquid is drained away from the upstream rim, droplet surface deformation by the inertial forces is minimized, thereby facilitating the restoring effects of the interfacial forces. This is manifested by the temporal reduction of the local curvature ($T^* = 1.02$ and 1.71) of the corresponding trough of the capillary wave (marked in blue) which is illustrated in Fig. 7. As time precedes, this trough collapses at $T^* = 2.4$, during which the interface assumes a linear shape which constitutes the tail of the droplet. With a continuous supply of wall momentum along the downstream direction, the tail of the droplet incurvates at $T^* = 3.08$, leading to the formation of local curvature on the interface. In contrast, the trough of the capillary wave near the downstream rim (marked in red) sustains for a longer time. As the inertial forces are supplemented by the momentum diffusion from the moving wall leading to higher surface deformation, the height of the trough decreases from $T^* = 1.02$ to 1.71. Surface tension forces begin to dominate as we notice an increase in the local

curvature ($T^* = 1.71$–2.4) of the downstream rim due to a greater influx of the droplet liquid. Consequently, the height of the trough increases, attains a maximum resulting in the collapse of the downstream trough of the capillary wave. It is to be noted that the increase in Laplace pressure due to the negative curvature of the trough ($T^* = 2.4$) amplifies its collapse.

The propagation of the capillary wave shown in Fig. 7 clearly illustrates the breakup in the symmetry of the wave motion on the droplet-free surface. For the stationary case, the two troughs of the wave propagate toward each other with equal speeds and collapse at the same point. However, when the surface moves with a constant velocity, the capillary wave does not converge radially inward and undergoes dissipation at different points along the droplet-free surface. The asymmetry in flow field inside the droplet and propagation of the capillary wave traveling wave on its free surface depends on the momentum imparted by the moving wall to the impinging droplet. This in turn depends on the magnitude of wall velocity (U_w). Figure 8(a) illustrates the temporal evolution of the spread factor (D^*) for different wall velocities. During the initial duration of the impact process, we observe that D^* is independent of U_w. This is attributed to the fact that the momentum possessed by the droplet during its inertial spreading phase is much higher than that supplied to the droplet by the moving wall. This behavior complements the temporal evolution of the total kinetic energy and surface
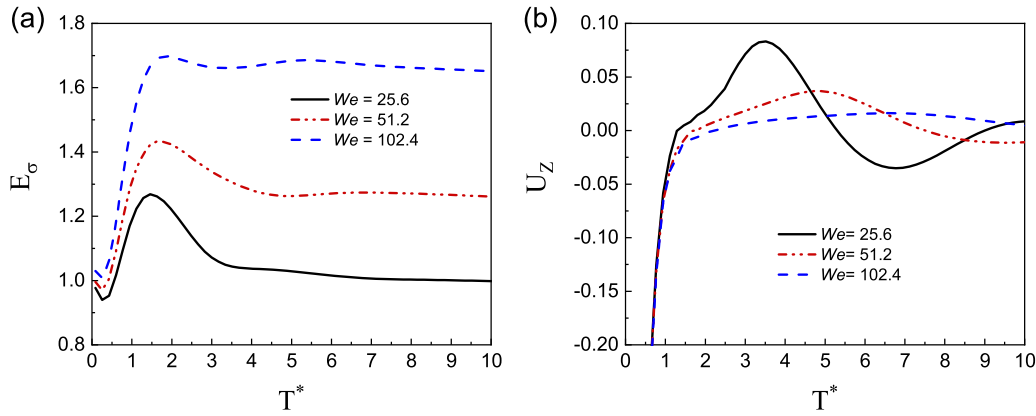
FIG. 9. Time evolution of (a) surface energy (E_σ) and (b) vertical component of velocity (U_z) for different Weber numbers (We) with Re = 600, $U_w = 0.075$, and surface contact angle $\theta = 90°$.

energy inside the droplet during the inertial phase as illustrated in Figs. 8(b) and 8(c), respectively. However, when the droplet slows down as it reaches its maximum spread, the role momentum supplied by the moving wall on the impact dynamics becomes prominent. The temporal evolution of the kinetic energy [Fig. 8(b)] illustrates that the inertial forces inside the droplet increase with an increase in U_w. This gives rise to an increased deformation of the droplet surface area which corresponds to the increase in E_σ with time as U_w increases. We notice that as time proceeds, D^* for the case with $U_w = 0.125$ decreases at a faster rate than other cases considered in this section. Since the droplet surface deformation during its recoiling phase is higher than the other cases, the conversion of E_σ into KE is also higher. This leads to an increase in the recoiling rate of the droplet.

We now understand that the magnitude of the momentum diffusion from the moving wall into the impinging droplet depends on the wall velocity. This, in turn, governs the asymmetry induced in droplet deformation and flow field. However, the extent to which the wall momentum influences the impact dynamics is inhibited by the restoring and resisting effects of surface tension and viscous forces acting on the droplet, respectively. We now turn our attention to the effects of these forces on the droplet impact dynamics.

C. Role of fluid properties: Surface tension and viscosity

The nature of surface tension force is to resist the formation of new surfaces as the impinging droplet undergoes spreading due to inertial forces. For a given U_w, the momentum supplied by the moving wall to the impinging droplet is fixed. During the inertial spreading phase ($T^* = 1.0$), due to the dominating influence of the initial kinetic energy of the impacting droplet, this resistance on droplet spreading is independent of the surface tension. However, as σ decreases, the resistance offered by the peripheral rims to the influx of droplet liquid decreases, thereby leading to higher surface deformation of the spreading droplet. Hence, the momentum transfer between the wall and the droplet liquid increases. This is illustrated in Fig. 9(a) which shows the temporal evolution of E_σ for different We obtained by varying the value of surface tension. The maximum value of E_σ increases with an increase in We. We observe that this trend in the evolution

of E_σ for varying We continues as time precedes. The rate of decrease in E_σ, after it reaches its maximum, decreases with increasing We with E_σ being nearly the same value for We = 102.4. This is attributed to the fact that a higher value of σ facilitates the reduction in droplet surface area as it under goes recoiling. To further elucidate the behavior of surface tension forces on the dynamics of droplet motion, we illustrate the temporal evolution of U_z in Fig. 9(b). Positive and negative values of U_z correspond to the droplet recoiling and spreading, respectively. Under the influence of increased capillary forces for We = 25.6, the droplet undergoes primary recoiling between $T^* = 1$ and $T^* = 5$, followed by secondary spreading and recoiling. These oscillations in U_z illustrate the competing dynamics of the restoring surface tension forces against the inertial forces which are supplemented by the wall momentum. As We increases, we notice that the amplitude of these oscillations in U_z reduces. For We = 102.4, we observe that the value of U_z remains close to zero after its inertial spreading, signifying that the inertial forces primarily dominate the receding droplet dynamics.

The shear deformation of a fluid element is resisted by the viscous stresses acting on it. Thus, increase in dynamic viscosity of the fluid will inhibit the inertia-driven droplet spreading as illustrated from the temporal evolution of A^* shown in Fig. 10(a) for varying Ohnesorge numbers (Oh). While we observe that the maximum A^* (A^*_{max}) is lowest for the case with Oh = 0.1431, the minimum A^*_{max} is noted for Oh = 0.0715 instead of the least viscous case with Oh = 0.0119. At the later stages of inertial spreading, the droplet slows down, and the restoring effects of surface tension forces commence flow reversal inside the droplet. For Oh = 0.0119, the weak viscous forces are unable to resist this flow reversal and undergo rapid recoiling when compared with other cases as shown in Fig. 10(a). However, supplemented by the wall momentum, the viscous forces for the case with Oh = 0.0715 resist the surface tension–driven flow reversal, and the droplet continues to undergo inertial spreading exceeding the maximum value of A^* for the case with Oh = 0.0119. The damping influence of viscous stress is further elucidated in Fig. 10(b) which shows the temporal evolution of U_z for different Oh. For Oh = 0.0119, U_z shows oscillatory behavior while the velocity profile for the case with Oh = 0.1431 is dampened by viscous stresses and does not exhibit any oscillations.
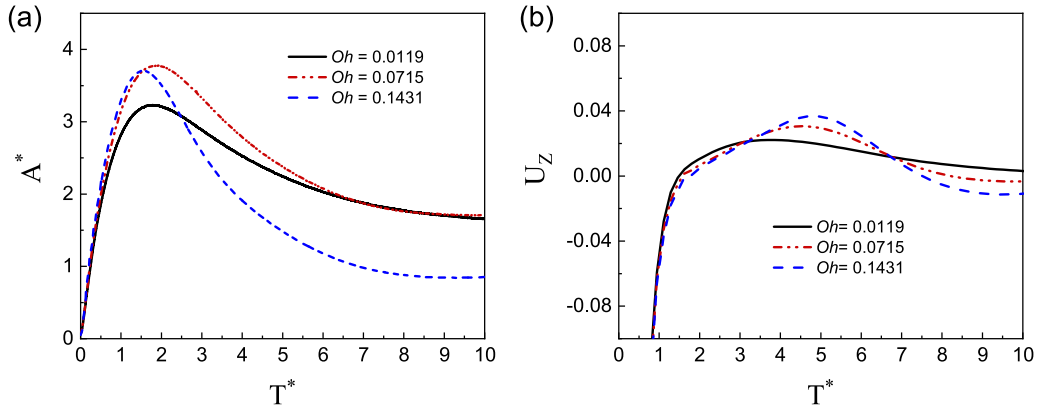
FIG. 10. Temporal evolution of the (a) contact area (A^*) and (b) volume-averaged vertical component of droplet velocity (U_z) for different Ohnesorge numbers (Oh) to investigate the effect of drop viscosity. The Webers number, wall velocity, and surface contact angle were set to be We $= 51.2$, $U_w = 0.075$, and $\theta = 90°$, respectively.

While the physiochemical factors, such as the surface contact angle, influence the area covered of the impinging droplet and therefore the momentum supplied by the moving wall, physical factors, such as the angle of impact, regulate the droplet impingement dynamics on moving walls. The interplay between the supplied wall momentum and anisotropic mass distribution inside the droplet originating from the contribution of tangential component of impact velocity leads to different spreading and recoiling dynamics. To investigate this, we next focus on oblique droplet impingement dynamics on moving dry surfaces.

D. Oblique droplet impingement dynamics

We begin our investigation by considering situations in which the directional sense of the tangential component of the impact velocity ($U_{||}$) is *inline* with the wall velocity. The wall velocity and surface contact angle are set to be 0.075 and 90°, respectively. Figure 11 shows the snapshots of the droplet impact sequence at different time steps with impact angle $\alpha = 30°$ (left column) and $\alpha = 60°$ (right column). At $T^* = 1.026$, we observe that the droplet initially deposits and spreads like an elongated pancake due to the tangential velocity component for $\alpha = 30°$. During this inertial phase of the impact process, the spreading dynamics is primarily governed by the impact velocity whose effect dominates the momentum supplied by the moving wall. As time proceeds, assisted by the wall motion and restoring effects of surface tension forces, the droplet liquid propagates from the trailing edge to the leading rim. Facilitated by the receding trailing edge, accumulation of the droplet liquid leads to increased thickness of the leading rim ($T^* = 1.71$–2.736) and increases the droplet height ($T^* = 5.814$). With the kinetic energy inside the droplet being converted into surface energy and a fraction of it being dissipated due to viscous effects, the droplet height decreases at $T^* = 8.208$. The role of the tangential component of impact velocity on the droplet morphology becomes more prominent as α increases. Instead of an elongated pancake shape which is observed for the case with $\alpha = 30°$ at $T^* = 1.026$, we notice an *inclined satellite*–shaped droplet morphology. As α increases, the tangential component of the impact velocity increases leading to greater influx of droplet

liquid along the tangential direction. The *crashing time*, which is the time taken by the droplet to undergo maximum spread, is delayed and anisotropy in the droplet shape is observed during its inertial spreading phase. A distinct difference in the two cases considered here is observed in the formation of the leading rims. The thickness of the leading rim for $\alpha = 30°$, which is in contact with the surface, is increased due to the accumulation of droplet liquid transported from both the $U_{||}$ and wall momentum due to U_w. However, for $\alpha = 60°$, the leading lamella is entirely lift-off from the surface and continues to elongate along the streamwise direction. Due to the reduction in the normal component of the impact velocity, the central region of the droplet undergoes delayed maximum spread ($T^* = 1.710$). This leads to the pumping of the droplet liquid into the elongating lamella and the formation of peripheral rims with large local curvatures. As surface tension forces begin to control of the recoiling dynamics, the elongated lamella thickens and grows in height, as observed at $T^* = 2.736$. Supplemented by the increased recoiling of the rear end, which is in contact with the moving wall, the peripheral rims coalesce, and the droplet acquires a shape of a slanted cylinder with a spherical top. The increase in droplet height with increasing α is illustrated by observing the temporal evolution of the contact area as shown in Fig. 11(b). As α increases, the normal component of the impact velocity decreases. This leads to the reduction in the initial droplet momentum along the z direction, and thereby the droplet covers lesser contact area during its inertial spreading phase. This is illustrated in Fig. 11(b) as the maximum A^* decreases with an increase in α. Due to volume conservation, the height of the droplet decreases with an increase in the impact angle. While we observe that for the cases with $\alpha = 0°$, $30°$, and $45°$, A^* converges to the same value as time proceeds, the temporal evolution of A^* for $\alpha = 60°$ deviates from this behavior. To delve deeper into this deviation, we probe the temporal evolution of the volume-averaged z component of droplet velocity as shown in Fig. 11(c). Compared to all other considered cases which follow a similar trend in U_z, the temporal evolution of U_z for $\alpha = 60°$ shows a sharp increase in U_z from $T^* = 3$–6. Hence, due to the high momentum of the droplet liquid along the z direction, the droplet elongates as a vertical columnlike structure with a smaller contact area. This increase in fluid
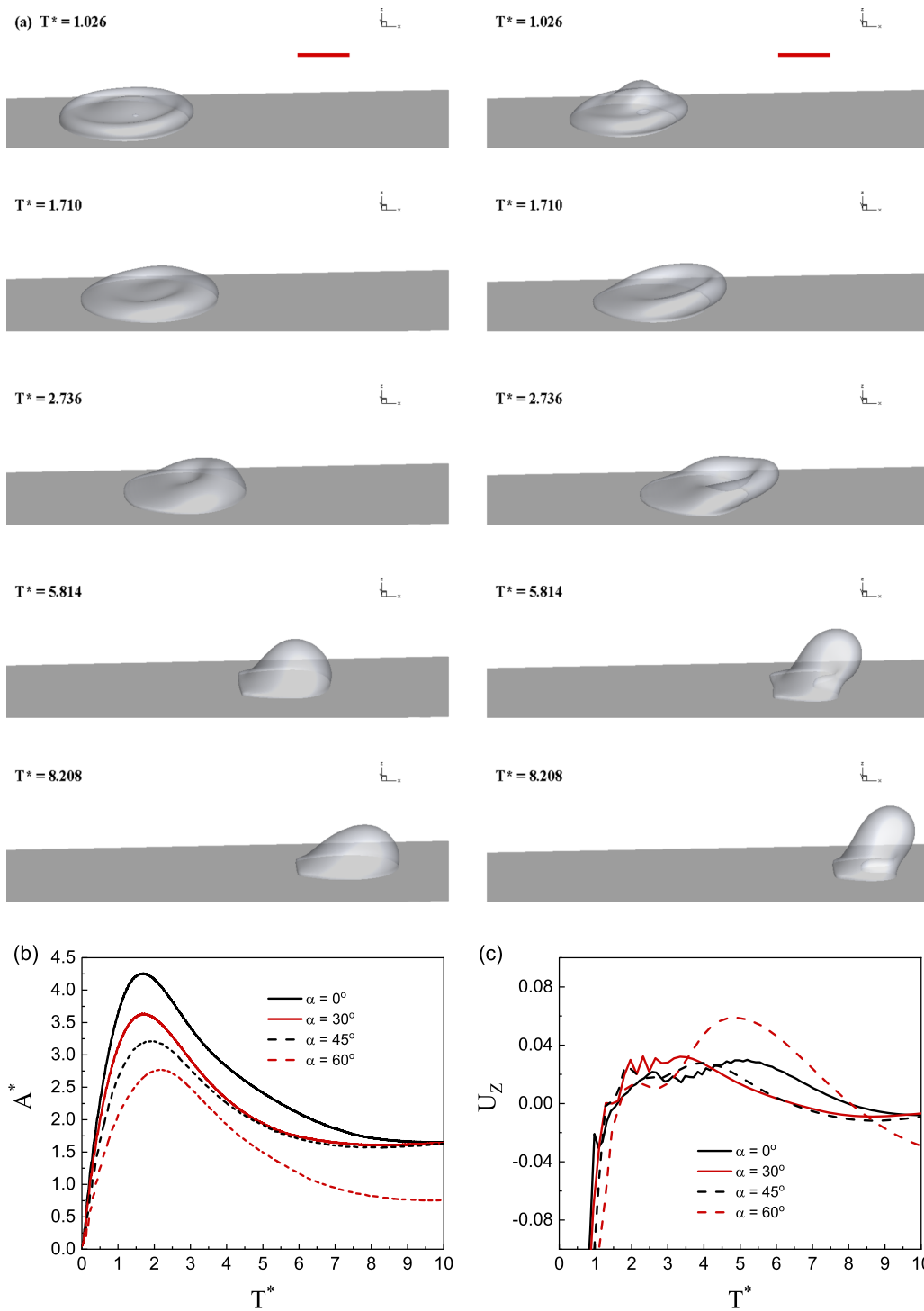
FIG. 11. (a) Snapshots of oblique *inline* droplet impingement on substrates with different impact angles: $\alpha = 30°$ (left column) and $\alpha = 60°$ (right column). The scale bar is 50 lattice units. Temporal evolution of the (b) contact area (A^*) and (c) volume-averaged vertical component of droplet velocity (U_z) for different impact angles (α) with the *inline* configuration. For all the cases, the wall velocity and surface contact angle are fixed at $U_w = 0.075$ and $\theta = 90°$, respectively. The line colors are assigned as (i) black (online and printed versions), (ii) red (online version), and gray (printed version).

momentum along the z direction is attributed to the increase in surface energy of the droplet during its recoiling phase. As mentioned before, the curvature of peripheral rims of the elongated leading lamella increases as the droplet liquid is pumped in from the region as shown in Fig. 11(a) at $T^* = 1.710$. This increase in interfacial curvature leads to intense

recoiling of the droplet system. However, instead of recoiling in a direction parallel to the wall, the momentum supplied by the moving wall, and the motion of the receding trailing edge divert the fluid motion along the vertical direction. This results in the formation of a slanted columnlike droplet morphology, as observed at $T^* = 5.814$ and 8.208.
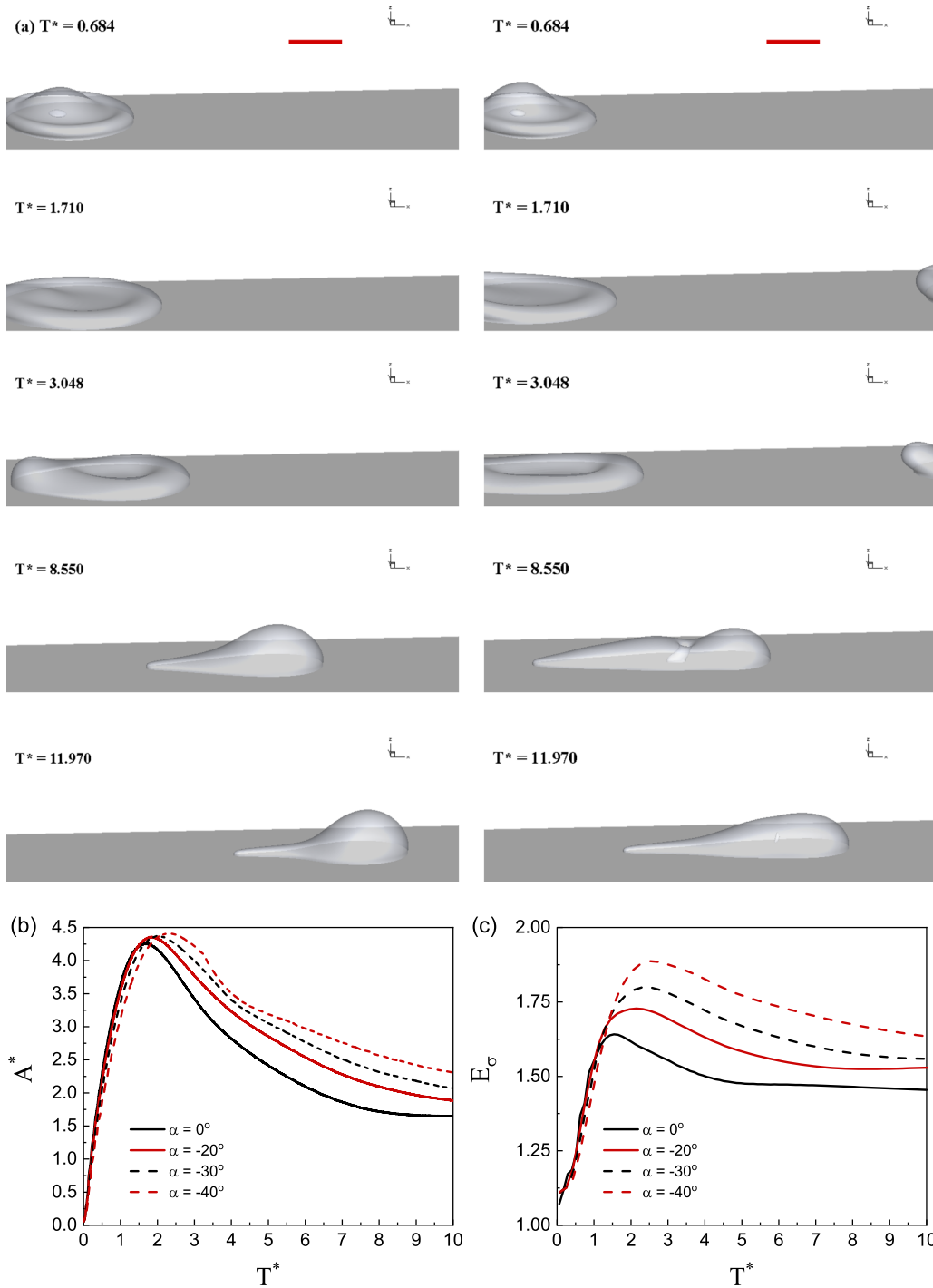
FIG. 12. (a) Snapshots of oblique *opposing* droplet impingement on substrates with different impact angles: $\alpha = -20°$ (left column) and $\alpha = -40°$ (right column). The scale bar is 50 lattice units. Time evolution of the (b) contact area (A^*) and (c) surface energy (E_σ) of the impinging droplet for different impact angles (α) with the *opposing* configuration. For all the cases, the wall velocity and surface contact angle are fixed at $U_w = 0.075$ and $\theta = 90°$, respectively. The line colors are assigned as (i) black (online and printed versions), (ii) red (online version), and gray (printed version).

We next investigate the situation wherein the impact angle is negative. The negative impact angle implies that the tangential component of the impact velocity has an *opposite* directional sense when compared to the wall velocity. Figure 12(a) illustrates the temporal evolution of droplet impaction dynamics on a moving wall with $\alpha = -20°$ (left column) and $-40°$ (right column), respectively. Similarly to the observations for the *inline* cases, during the early stages of the impact process, we observe an asymmetry in the droplet shape at $T^* = 0.684$. However, due to the direction of the tangential velocity component, the spreading lamella with a higher curvature is formed on the upstream side of the moving

wall. As time progresses, the deviation of droplet morphology from the *inline* configuration becomes more prominent. The moving wall continues to supply momentum to the droplet liquid, close to the wall region, in the downstream direction. This leads to the temporal growth in the thickness of the downstream rim. At the same time, due to the tangential component of the impact velocity, the upstream lamella continues to propagate along the upstream direction. This movement of the downstream and upstream rims in opposite directions results in the stretching and elongation of the droplet system along the wall parallel direction as observed at $T^* = 1.710$ and 3.048. The elongation is dependent on the impact angle, which governs the magnitude of the initial tangential momentum of the impinging droplet. It is to be noted that unlike the *inline* configuration where a single growing downstream rim primarily characterizes the downstream rim after the crashing time, as shown in Fig. 11(a) at $T^* = 1.710$ and 2.736, the *opposing* case is delineated by two rims of varying curvature even at high impact angles. At $T^* = 3.048$, the upstream rim formed for the case with $\alpha = -20°$ is in contact with the moving wall, whereas the upstream rim for $\alpha = -40°$ is lift-off from the surface. As the momentum is continuously supplied from the moving wall along the downstream direction and facilitated by the surface tension effects, the rear end begins to recoil, and the droplet liquid propagates from an upstream to a downstream direction. This motion combined with the upward recoiling of the flattened central region results in the growth of droplet height ($T^* = 8.550$ and 11.970). The onset of this recoiling motion and reversal in the direction of fluid motion inside the droplet is delayed with an increase in the magnitude of α. This is observed from the droplet shapes observed at $T^* = 8.550$ and 11.970. For the case with $\alpha = -40°$, the droplet surface is more streamlined and flattened along the direction of wall motion. The interface shape for $\alpha = -20°$ is blunter on the front side and shows a sharp transition, leading to the formation of a tail structure on the rear end. This formation of a sharp tail structured rear end for *opposing* cases is a distinct feature which is not observed for the *inline* impact scenarios at a given contact angle. This is attributed to the reversal in the flow direction inside the droplet during the recoiling phase of the *opposing* oblique droplet impact situations. The temporal evolution of the contact area (A^*) shown in Fig. 12(b) quantifies the stretching and elongating behavior of the droplet which is amplified as the absolute value of the impact angle increases. During the initial stages of impact, we observed that A^* is primarily dependent on the normal component of the impact velocity. Therefore, during its inertial spreading phase, A^* increases as α magnitude decreases. Nevertheless, as the two end of the droplet continue to propagate in the opposite direction and lead to droplet stretching along the direction of wall motion, A^* increases with an increase in the absolute value of α. It is to be noted that we observe a reversal in trend for the temporal evolution A^* for *opposing* cases when compared with the *inline* configuration. In the latter case, an increase in α leads to droplet elongation along the wall-normal direction, whereas droplet elongation is mainly along the wall movement direction for the *opposing* impact scenarios. This increase in the surface area on the impinging droplet is complemented by the temporal evolution of the surface energy (E_σ) for different impact angles shown

in Fig. 12(c). As the absolute value of α increases, the surface energy of the droplet system increases, signifying the increase in surface area of the elongating droplet.

V. CONCLUSIONS

We have performed a three-dimensional numerical investigation of a droplet impacting on a smooth dry moving solid surface. A high-density ratio-based phase-field lattice Boltzmann method is employed in conjunction with a geometric-based contact line formulation for the moving contact line. The results from this work indicate rich morphology in droplet interface profiles when compared to those of droplet impingement on stationary surfaces. An elongated tail like structure is observed at the trailing end of the recoiling droplet, the end of which becomes sharper as the contact angle increases. The impinging droplet is discerned to lift off obliquely from a moving hydrophobic surface. The momentum imparted by the moving wall is found to induce a flow diversion from the central region toward the downstream direction, giving rise to symmetry breaking during the spreading and recoiling phases of the droplet impingement process. Furthermore, we elucidate the propagation mechanism of the capillary waves traveling along the droplet-free surface when it impinges onto a stationary and moving surface. The troughs of the propagating capillary waves was found to collapse into each other when the drop impacts onto a stationary surface, whereas they are observed to dissipate at different locations and time instants when impinged onto a moving surface. For the first time, we analyzed oblique droplet impingement dynamics on moving dry surfaces. For the *inline* droplet impact situations, at higher impact angles, the momentum supplied by the moving wall assists in the diversion of the receding droplet liquid along upward direction, resulting in the formation of a slanted and elongated droplet structure. However, for the *opposing* impact scenarios, we notice droplet stretching along the direction parallel to the moving wall which is characterized by the formation of two distinct rims at the upstream and downstream directions. Unlike the *inline* case, the recoiling phase of droplet impingement in *opposing* impact situations is always characterized by a tail like structure. The current study suggests that, apart from the spreading phase, the momentum supplied by the moving wall plays a vital role in the receding dynamics. The understanding of recoiling dynamics of the droplet, especially in complex situations like oblique impingement, is pivotal when it further interacts and coalesces with neighbor impinging drops as encountered in several industrial applications. While we focus on presenting the underlying flow physics when a droplet impinges onto a moving dry surface in this work, a detailed parametric study on the droplet impact outcomes on moving surfaces for different Reynolds number and Weber number is an important scope for future work. Regime maps and correlations constructed from such a case study could be used directly in practical applications.

[1] S. Fathi and P. Dickens, J. Mater. Process. Technol. **213**, 84 (2013).

[2] A. M. Worthington, *A Study of Splashes* (Longmans, Green and Co., London, 1908).

[3] I. Roisman, J. Fluid Mech. **656**, 189 (2010).

[4] J. Eggers, M. A. Fontelos, C. Josserand, and S. Zaleski, Phys. Fluids **22**, 062101 (2010).

[5] S. Mandre, M. Mani, and M. P. Brenner, Phys. Rev. Lett. **102**, 134502 (2009).

[6] R. Rioboo, M. Marengo, and C. Tropea, Exp. Fluids **32**, 112 (2002).

[7] I. Roisman and C. Tropea, J. Fluid Mech. **472**, 373 (2002).

[8] G. Cossali, M. Marengo, A. Coghev, and S. Zhdanov, Exp. Fluids **36**, 888 (2004).

[9] D. Weiss and A. Yarin, J. Fluid Mech. **385**, 229 (1999).

[10] H. Shetabivash, F. Ommi, and G. Heidarinejad, Phys. Fluids **26**, 012102 (2014).

[11] J. Fukai, Y. Shiiba, T. Yamamoto, O. Miyatake, D. Poulikakos, C. Megaridis, and Z. Zhao, Phys. Fluids A **7**, 236 (1995).

[12] T. Lee and L. Liu, J. Comput. Phys. **229**, 8045 (2010).

[13] C. Josserand and S. Zaleski, Phys. Fluids **15**, 1650 (2003).

[14] M. Rein, Fluid Dynam. Res. **12**, 61 (1993).

[15] K. Raman, R. Jaiman, T. Lee, and H. Low, Int. J. Heat Mass Transf. **95**, 336 (2016).

[16] P. Unnikrishnan, V. Vaikuntanathan, and D. Sivakumar, Colloids Surf. A **459**, 109 (2014).

[17] K. Raman, J. Colloid Interface Sci. **516**, 232 (2018).

[18] V. Vaikuntanathan, R. Kannan, and D. Sivakumar, Colloids Surf. A **369**, 65 (2010).

[19] M. Reyssat, F. Pardo, and D. Quere, Europhys. Lett. **87** (2009).

[20] J. Zhao and S. Chen, Langmuir **33**, 5328 (2017).

[21] J. Hao and S. Green, Phys. Fluids **29**, 012103 (2017).

[22] J. C. Bird, S. S. H. Tsai, and H. A. Stone, New J. Phys. **11**, 06317 (2009).

[23] H. Almohammadi and A. Amirfazli, Soft Matter **13**, 2040 (2017).

[24] Z. Xie, G. Hewitt, D. Pavlidis, P. Salinas, C. Pain, and O. Matar, Chem. Eng. Sci. **166**, 303 (2017).

[25] C. Ming and J. Lou, Comput. Math. Appl. **67**, 307 (2014).

[26] K. Raman, R. K. Jaiman, T. Lee, and H. Low, Comput. Fluids **107**, 285 (2015).

[27] F. Chou, T. Zen, and K. Lee, Atom. Sprays **19**, 905 (2009).

[28] T. Zen, F. Chou, and J. Ma, Int. Commun. Heat. Mass Transf. **37**, 1025 (2010).

[29] K. A. Raman, R. K. Jaiman, Y. Sui, T.-S. Lee, and H.-T. Low, Phys. Rev. E **94**, 023108 (2016).

[30] P. Lallemand and L. Luo, J. Comput. Phys. **184**, 406 (2003).

[31] T. Lee and C. Lin, J. Comput. Phys. **206**, 16 (2005).

[32] T. Inamuro, T. Ogata, S. Tajima, and N. Konishi, J. Comput. Phys. **198**, 628 (2004).

[33] X. He, X. Shan, and R. Zhang, J. Comput. Phys. **152**, 642 (1999).

[34] H. Zheng, C. Shu, and Y. Chew, J. Comput. Phys. **218**, 353 (2006).

[35] H. Ding and P. D. M. Spelt, Phys. Rev. E **75**, 046708 (2007).

[36] K. Raman, R. Jaiman, T. Lee, and H. Low, Chem. Eng. Sci. **145**, 181 (2016).

[37] K. Raman, R. Jaiman, T. Lee, and H. Low, J. Colloid Interface Sci. **486**, 265 (2017).

[38] Y. Sui, H. Ding, and P. Spelt, Annu. Rev. Fluid Mech. **46**, 97 (2014).

[39] Y. Renardy, S.Poipnet, L. Duchemin, M. Renardy, S. Zaleski, C. Josserand, M. A. Drumright-Clarke, D. Ruchard, C. Clanet, and D. Quere, J. Fluid Mech. **484**, 69 (2003).